

# BORON NANOWIRES AND NOVEL *TUBE-CATALYTIC PARTICLE-WIRE* HYBRID BORON NANOSTRUCTURES

TERRY T. XU\*

*Department of Mechanical Engineering, Northwestern University  
2145 Sheridan Road, Evanston, IL 60208, USA  
ttxu@uncc.edu*

ALAN W. NICHOLLS

*Research Resource Center, University of Illinois at Chicago  
845 West Taylor Street, Chicago, IL 60607, USA  
nicholls@uic.edu*

RODNEY S. RUOFF†

*Department of Mechanical Engineering, Northwestern University  
2145 Sheridan Road, Evanston, IL 60208, USA  
r-ruoff@northwestern.edu*

Received 13 March 2006

Revised 17 April 2006

Catalyst-assisted growth of boron nanowires and novel *tube-catalytic particle-wire* hybrid boron nanostructures were achieved by pyrolysis of diborane at 820–890°C and  $\sim 200$  mTorr in a quartz tube furnace. Electron microscopy imaging and diffraction analysis reveal that most of the nanostructures are amorphous. Elemental analysis by EELS and EDX shows that the nanostructures consist of boron with a small amount of oxygen and carbon. Possible growth mechanisms for the *tube-catalytic particle-wire* hybrid boron nanostructures are discussed.

*Keywords:* Boron nanowires; boron nanotubes; hybrid nanostructures; chemical vapor deposition; diborane; electron microscopy.

## 1. Introduction

Boron (B) is an element that exhibits structural complexity due to its electron-deficient bonds.<sup>1–3</sup> Extensive fundamental and applied research of boron and boron-rich materials has been reported, for example in Refs. 1 and 2. Elemental boron has an unusual combination of properties, including high melting point ( $\sim 2200^\circ\text{C}$ ), low density ( $2.340\text{ g/cm}^3$ ), moderate oxidation resistance, high

hardness (Knoop: 2160–2900), high Young's modulus (380–400 GPa),<sup>4,5</sup> and interesting optical and electrical properties.<sup>1</sup> The element boron is used in high-temperature devices, in nuclear engineering due to the high neutron capture cross-section, as a high-energy fuel, in coatings, and in other applications.<sup>1</sup>

The theoretical prediction of metallic single-walled nanotubes of either pure boron<sup>6–9</sup> or aluminum boride ( $\text{AlB}_2$ )<sup>10</sup> motivates attempts

\*Present address: Department of Mechanical Engineering and Engineering Science, The University of North Carolina at Charlotte, Charlotte, NC 28223, USA.

†Corresponding author.

to synthesize boron and metal boride one-dimensional (1D) nanomaterials. For example, boron nanowires,<sup>11–17</sup> nanobelts,<sup>18</sup> and nanoribbons<sup>19</sup> have been synthesized by magnetron sputtering, laser ablation, and chemical vapor deposition (CVD). Metal boride 1D nanostructures such as chromium boride (CrB) nanorods,<sup>20</sup> magnesium diboride ( $\text{MgB}_2$ ) nanowires,<sup>21–23</sup> and calcium hexaboride ( $\text{CaB}_6$ ),<sup>24</sup> lanthanum hexaboride ( $\text{LaB}_6$ ),<sup>25</sup> cerium hexaboride ( $\text{CeB}_6$ )<sup>26</sup> and gadolinium hexaboride ( $\text{GdB}_6$ )<sup>27</sup> nanowires have also been synthesized. Compared to the worldwide efforts underway on carbon nanotubes (CNTs) and nanofibers, systematic work on synthesis and characterization of boron-rich nanostructures is still at an early stage.

By using a home-built low pressure chemical vapor deposition (LPCVD) system and diborane ( $\text{B}_2\text{H}_6$ ) as precursor, we have successfully synthesized  $\alpha$ -tetragonal boron nanoribbons<sup>19</sup> and  $\text{CaB}_6$  nanowires.<sup>24</sup> In this report, we present the catalyst-assisted growth of boron nanostructures by pyrolysis of  $\text{B}_2\text{H}_6$  at 820–890 °C and  $\sim 200$  mTorr. Particles of gold (Au), and from a platinum (Pt)/palladium (Pd) alloy, were found to be effective catalysts. In addition to amorphous and  $\alpha$ -tetragonal boron nanowires, novel “*tube-catalytic particle-wire*” hybrid boron nanostructures were discovered. Both boron nanowires and hybrid boron nanostructures have potential applications in nanocomposites, nanoelectronics, and others. To our knowledge, this is the first report of *tube-catalytic particle-wire* hybrid boron nanostructures. Understanding the growth mechanism(s) of these hybrid nanostructures would guide their controlled growth and perhaps lead to better methods for their synthesis.

## 2. Experimental Procedures

Our experiments were carried out in a home-built LPCVD system described elsewhere.<sup>19</sup> Silicon (Si) substrates with one-micron thick thermally grown  $\text{SiO}_2$  (University Wafer;  $1 \times 2 \text{ cm}^2$ ) were used for the experiments. These Si substrates were ultrasonically cleaned using acetone and ethanol (Crest ultrasonic cleaner; 5 min), followed by oxygen plasma cleaning (Plasma-862, Kurt J. Lesker; 3 min). A thin Au layer (2–3 nm) was then sputtered on the Si substrate (Cressington 208 HR sputter coater; 99.999% Au target from Ted Pella). The substrates were loaded in a quartz boat and placed in the

one-inch diameter quartz reaction tube. The temperature was ramped up to 900 °C (temperature at the center position of a six-inch “clam shell” furnace; Watlow) in 60 min with 15 sccm (standard cubic centimeters per minute) continuous flow of argon (BOC gases; 99.999% purity). A gas mixture of diborane (Voltaix; 5% UHP diborane in research grade argon; flow rate: 15 sccm) and argon (flow rate: 15 sccm) was then introduced into the chamber for 45 min. The reaction pressure for each run was  $\sim 200$  mTorr (for any particular run, the pressure was measured to three significant figures). After reaction, the chamber was cooled to room temperature in  $\sim 5$  h under 15 sccm argon flow. The substrates were taken out and characterized by scanning electron microscopy (SEM; LEO 1525 FE-SEM), transmission electron microscopy (TEM) including electron diffraction (Hitachi H-8100), high-resolution TEM (HR-TEM; Hitachi H-2000), electron energy loss spectroscopy (EELS; JEOL JEM 2010F) and energy dispersive X-ray spectroscopy (EDX; JEOL JEM 3010, JEOL JEM 2010F).

## 3. Experimental Results

Wire-like nanostructures were synthesized on the substrates placed in the  $\sim 4$  cm long zone of the reaction chamber having temperature in the range of 820–890 °C. Figure 1 is a representative SEM

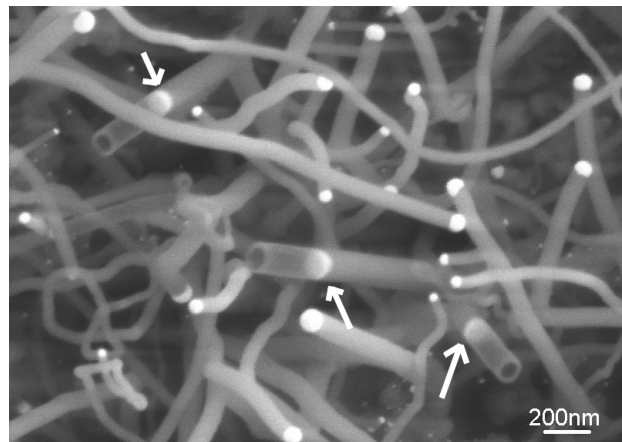


Fig. 1. SEM micrograph of as-synthesized boron nanostructures with two different morphologies. One is that of a nanowire with a catalytic particle (white in the image) on the tip. The other is that of a “*tube-catalytic particle-wire*” hybrid nanostructure (indicated by white arrows) with the catalytic particles located between the nanotube and nanowire segments.

micrograph of nanostructures with two different morphologies. One is nanowires with catalytic particles (which appear white in Fig. 1) on their tips, and the other is *tube-catalytic particle-wire* hybrid nanostructures (indicated by white arrows) with catalytic particles located between the nanotube and solid nanowire segments. These B nanostructures are typically 35–150 nm in diameter.

There have been several reports on synthesis of wire-tube hybrid nanostructures,<sup>28,29</sup> especially on semiconductor nanowire-CNT heterojunctions. A two-step synthesis process is commonly employed to create the hybrid nanostructures. For example, to create Si nanowire-CNT heterojunctions,<sup>29</sup> the Si nanowires were first synthesized by a catalytic process based on what was likely the vapor-liquid-solid (VLS) mechanism.<sup>30</sup> The Fe catalysts which naturally localized at the ends of the Si

nanowires were then used to direct the growth of CNTs using a hydrocarbon reactant. Different from these wire-tube heterojunctions, the *tube-catalytic particle-wire* hybrid nanostructures reported here were synthesized by a one-step process. In addition, both the tube and wire segments were made of boron.

Figures 2(a)–2(f) show TEM/EDX/EELS results of the as-synthesized boron nanostructures. Figure 2(a) is a TEM micrograph of a nanowire with a catalytic particle at the tip. Electron diffraction analysis and high-resolution TEM (HR-TEM) imaging (results not shown here) showed that the nanowire is amorphous. Figure 2(b) is a TEM micrograph of a crystalline nanowire. The inset shows the corresponding diffraction pattern. Based on our examination of fifty nanowires, about 90% of them were amorphous. Therefore,

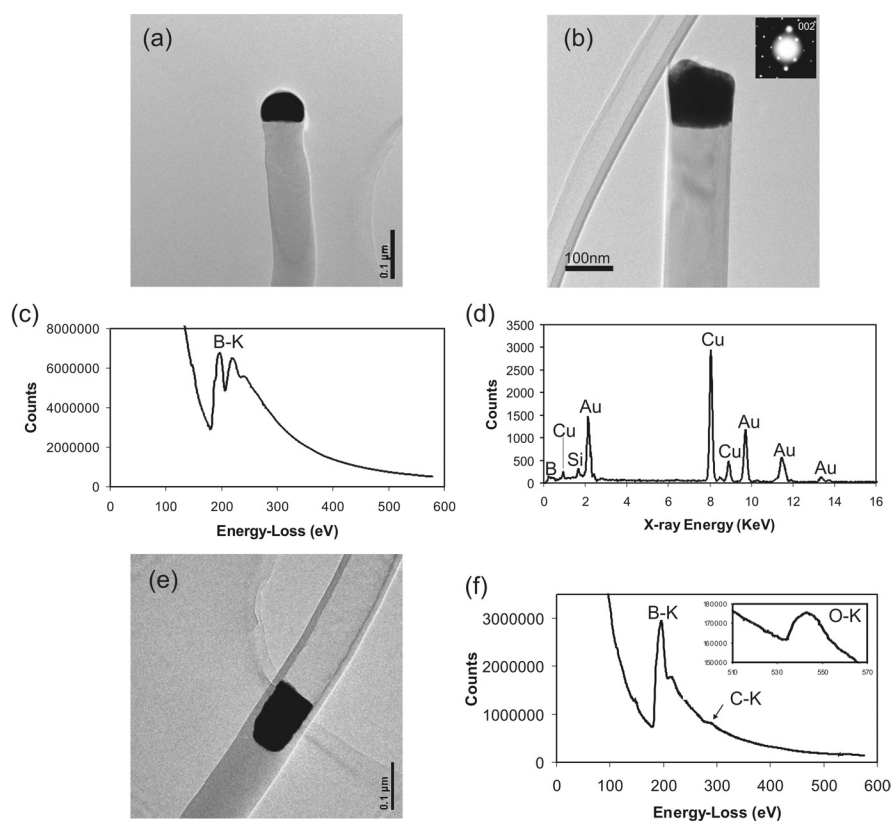


Fig. 2. (a) A TEM image of a part of one amorphous boron nanowire. A hemispherical catalytic particle is present at the tip of the nanowire. (b) A TEM image of a part of one crystalline boron nanowire. The inset shows the corresponding diffraction pattern from the nanowire. (c) An EELS spectrum recorded from one amorphous nanowire, showing the B K-shell ionization edge at  $\sim 188$  eV. (d) An EDX spectrum from one catalytic particle, showing the presence of Au, Si and B. (e) A TEM image of a part of one *tube-catalytic particle-wire* hybrid nanostructure. The catalytic particle is located between the tubular and wire segments. Note that the particle has a different shape than in (a) and (b). (f) An EELS spectrum recorded from the tubular portion of one *tube-catalytic particle-wire* hybrid nanostructure, showing the high-intensity B K-shell ionization edge at  $\sim 188$  eV, and weak C K-shell ionization edge at  $\sim 284$  eV. The inset shows the extremely small intensity O K-shell ionization edge at  $\sim 532$  eV. The scale bars in (a), (b) and (e) represent 100 nm.

the amorphous nanowires are our main focus of discussion in this paper. Figure 2(c) is an EELS spectrum of one amorphous nanowire, showing the strong boron K-shell ionization edge at  $\sim 188$  eV. Because the nanowire is relatively thick ( $\phi$ :  $\sim 90$  nm), the B K-shell ionization edge shows evidence of multiple scattering with a plasmon peak superimposed. There is no detectable carbon (C) or oxygen (O) K-shell ionization edges that would appear at  $\sim 284$  eV and  $\sim 532$  eV, respectively. However, it is possible that trace amounts of C and O (below the detection limit of EELS) exist in the nanowire (as discussed further in later text). Figure 2(d) is a representative EDX spectrum recorded from one catalytic particle, from which Au, Si, B, and Cu are identified (the Cu signal comes from the supporting Cu grid and is not a component of the nanowire). From the TEM/EELS/EDX analysis, most of the as-synthesized nanowires are amorphous B-rich nanowires. The hemispherical catalytic particles consist of Au, Si and B.

Figure 2(e) shows a TEM image of a *tube-catalytic particle-wire* hybrid nanostructure. The catalytic particle, with hemisphere shape, is located between the wire and tube portions. The tube outer diameter is  $\sim 115$  nm and the tube has a 14-nm thick wall. Like the boron nanowire discussed above, the *tube-catalytic particle-wire* hybrid nanostructure is also amorphous as identified by electron diffraction analysis and HR-TEM. EDX and EELS spectra were obtained to determine the composition of: the wire segment, the catalytic particle, and the tubular segment of the hybrid nanostructure. The wire segment and the catalytic particle in the hybrid nanostructure had a similar composition as that of the boron nanowire discussed previously, that is, the wire segment consists of B, and the catalytic particle is composed of Au, Si and B. The EELS spectrum obtained from the tubular segment (Fig. 2(f)) has a strong B K-shell ionization edge at  $\sim 188$  eV, and two weak C and O K-shell ionization edges at  $\sim 284$  eV and  $\sim 532$  eV, respectively. From the TEM/EELS/EDX analysis, the as-synthesized *tube-catalytic particle-wire* hybrid nanostructures are typically amorphous B-rich nanostructures with possible trace amounts of other elements in the wire segment, and detectable levels (by EELS) of C and O in the tubular segment. The catalytic particles consist of Au, B and Si.

Boron is a very reactive element.<sup>1–3</sup> It is very difficult to produce elemental boron in high purity;

the presence of different impurities has been identified in as-synthesized bulk B crystals, B thin films, and B 1D nanostructures.<sup>2,13,14,18,19,31</sup> For example, most of the B 1D nanostructures synthesized so far have been reported to have thin oxide surface layers.<sup>14,18,19</sup> The oxide layers can form either during the reaction process (B can react with O to form  $B_2O_3$  at oxygen partial pressure as low as  $6.8 \times 10^{-22}$  Pa),<sup>31</sup> or during the storage process (the surface of samples of B will oxidize in air and at room temperature).<sup>32</sup> It is also likely that such oxide surface coatings can be converted wholly or in part, to boric acid, particularly in relatively humid environments.<sup>33</sup> The presence of C in (or perhaps on) as-synthesized B nanowires has also been reported. Molecules containing carbon are likely to be adsorbed as a surface layer on B nanowires,<sup>13</sup> or C could, if present during synthesis, incorporate into B to stabilize, e.g., the  $\alpha$ -tetragonal B structure.<sup>34</sup> Both C and O are ubiquitous in the ambient environment.

The EELS result (Fig. 2(c)) from the B nanowire, and also from the wire segment of the B hybrid nanostructure, shows the presence of only B. The detection limit of EELS for C and O in the presence of B is however  $\sim 1$  atomic%. The EELS result (Fig. 2(f)) from the tubular segment of the B hybrid nanostructure reveals the existence of B and small amounts of C and O. If one assumes that C and O exist on the surface of the B nanostructures, it is reasonable that their concentration relative to B would be higher in the tubular segment because of its higher surface-to-volume ratio (note that there is an “outside” and an “inside” surface for the tube segment). For example, the ratio of surface area (SA) to volume (V) for a solid cylindrical rod of length  $L$  and radius  $r$  is  $2/r$ ; for a tube of length  $L$  and wall thickness  $t$  it is  $2/t$ . In our case, for the solid wire portion in the hybrid B nanostructure in Fig. 2(e), the SA/V ratio is  $3.48 \times 10^{-2} \text{ nm}^{-1}$ ; in the tube segment connected to the solid wire portion, the SA/V ratio is  $1.43 \times 10^{-1} \text{ nm}^{-1}$ .

In addition to Au, platinum (Pt)/palladium (Pd) alloy (80% Pt, 20% Pd, Refining Systems), and nickel (Ni, 99.99% purity, Goodfellow) were used as potential catalysts. Pt/Pd alloy particles catalyzed B nanostructures (both solid wires and hybrid *tube-catalytic particle-wire* structures), but Ni did not. The growth conditions (gas flows, pressure, and temperature) were identical to the

“Au” catalyst runs as mentioned above. Different substrate materials (sapphire and single-crystal quartz) were used in addition to the 1- $\mu\text{m}$  thick thermal oxide-on-Si wafer piece; boron nanostructures of (apparent) similar type grew on all three substrates. Finally, the diameter of boron nanostructures could be tuned by varying the thickness of the (catalytic) metal films, and the reaction time. Thinner catalytic films and shorter reaction times yielded smaller diameters. The smallest diameter B nanostructures had a diameter of  $\sim 8$  nm, as measured by SEM.

#### 4. Discussion on the Growth Mechanisms

The existence of a catalytic particle on the tip of each boron nanowire suggests that the growth is probably due to the vapor-liquid-solid (VLS) mechanism.<sup>30</sup> The major steps in the VLS growth are (1) deposition of B atoms on the surface of the metal (catalytic) particle, such as through decomposition of  $\text{B}_2\text{H}_6$  at the particle surface, and diffusion of B into the interior of the catalytic particle (in VLS, the catalytic particle is a liquid; in vapor-solid-solid (VSS) growth, the catalytic particle remains solid), (2) supersaturation of B in the catalytic particle (droplet) and precipitation of B at the liquid-solid interface, and (3) formation of B nanowires by continuous buildup of B at the liquid-solid interface.

In the VLS growth mechanism, the liquid droplets are usually low-melting-point eutectic alloys composed of (i) an element that is catalytic for surface decomposition of a gas phase precursor(s), and (ii) the element composing the solid phase. Pt and Pd form eutectic alloys with B at  $920^\circ\text{C}$  and  $964^\circ\text{C}$ ,<sup>35</sup> respectively, thus Pt and Pd are our choice of a conveniently available alloy. Au appears to form a eutectic alloy with B at  $1053 \pm 3^\circ\text{C}$  and  $< 5$  at.% B.<sup>36</sup> This higher temperature for the formation of a eutectic alloy between Au and B ( $\sim 250^\circ\text{C}$  higher than our experimental temperature) suggests that (at least at the growth temperature we employed) pure Au should not yield B nanowires or hybrid nanostructures as reported here, at least by the VLS growth mechanism. As mentioned for B nanowires<sup>21</sup> and  $\text{ZrB}_2$  whiskers,<sup>37</sup> small amounts of impurities are able to significantly broaden the temperature range for the growth of nanowires (that are probably growing by the VLS

mechanism). In our experiments, the impurity is Si as indicated by EDX analysis (Fig. 2(d)). Au reacts with Si to form a low-melting-point eutectic alloy at  $370^\circ\text{C}$ .<sup>35</sup> Therefore, it is possible that Au-Si liquid alloy droplets were formed and the B nanowires were grown from Au-Si-B. The Si might come from the  $\text{SiO}_2/\text{Si}$  substrates or quartz tubes. Croft *et al.* reported that B can possibly react with thermally-grown  $\text{SiO}_2$  at elevated temperatures ( $900^\circ\text{C}$ ) to yield volatile silicon monoxide (SiO) and boron trioxide ( $\text{B}_2\text{O}_3$ ).<sup>38</sup> Similarly, Ellis reported that B can react with a quartz tube to yield Si and  $\text{B}_2\text{O}_3$  at  $950^\circ\text{C}$ .<sup>39</sup> In our experiments, the pyrolysis of  $\text{B}_2\text{H}_6$  might yield highly reactive boron and hydrogen, which may influence the formation of gas phase Si-containing species (such as  $\text{SiH}_x$  radicals,  $x = 1$  to 3). These Si-containing species could in turn lead to the formation of Au-Si eutectic droplets.

When the substrate was changed from  $\text{SiO}_2/\text{Si}$  to sapphire and the reaction tube was simultaneously changed from quartz to alumina, EDX analysis revealed that the catalytic particles contained Au, B, and Al, indicating that Al-containing species formed by reaction between B and sapphire or the  $\text{Al}_2\text{O}_3$  tube could form low-melting-point Au-Al eutectic droplets ( $\sim 525^\circ\text{C}$ ) to facilitate the VLS growth of B nanowires.

Though the growth of amorphous B nanowires can be rationalized by the VLS mechanism, the growth mechanism(s) of the *tube-catalytic particle-wire* hybrid B nanostructures are not clear. Several questions, among others, can be asked. For example, when and how did the hybrid nanostructures form? As a consequence of reactive species such as  $\text{B}_2\text{H}_6$  or its decomposition gas phase products; or, for example, during the cooling stage under Ar? We present and discuss two hypotheses.

**Hypothesis 1.** The hybrid B nanostructures were formed during the presence of  $\text{B}_2\text{H}_6$  or its gas phase decomposition products, and the growth mechanism is a combination of tip-growth and root-growth mechanisms.

Tip-growth and root-growth mechanisms are two common mechanisms used to interpret the catalytic growth of CNTs.<sup>40</sup> In tip-growth mode, the catalytic particle is located on the tip of the growing NT. In root-growth mode, the catalyst is located at the NT base. Major steps involved in both growth mechanisms include the generation of C species (e.g., dehydrogenation of hydrocarbon precursor molecules), production of liquid

metal catalytic particles saturated with C, diffusion of C (both bulk diffusion and surface diffusion), and precipitation or segregation of C to form CNTs. Among these steps, the diffusion process is important for the selection of the NT growth mode.<sup>40</sup> It is generally accepted that: (a) if the time for bulk diffusion of C through the catalytic particle ( $t_b$ ) is longer than that of the surface diffusion of C around the catalytic particle ( $t_s$ ), the catalytic particle surface will saturate with C much faster than C will penetrate to its base. Hence, C will precipitate at the surface (or periphery) of the catalytic particle and the particle will remain on the substrate during the growth of the CNT (root-growth model, Fig. 3(b)). (b) If  $t_b$  is shorter than  $t_s$ , C will penetrate through the particle faster than saturation of the particle surface. The catalytic particle will remain on the tip of the NT (tip-growth mode, Fig. 3(c)).

Four major steps are related to Hypothesis 1: (i) Formation of amorphous boron nanowires. As discussed, amorphous boron nanowires could be formed according to the VLS (or tip-growth)

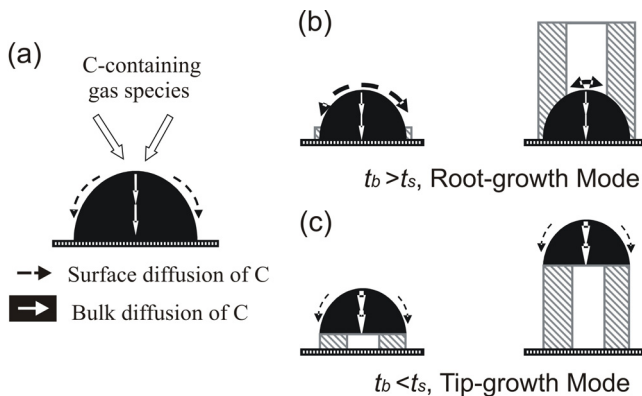


Fig. 3. Schematic of the difference between tip-growth and root-growth modes of growth of CNTs. (a) Saturation of a catalytic particle with C. There are two diffusion paths of C. One is bulk diffusion of C (white arrows) from the particle–surface (high C concentration) to the particle–substrate interface (low C concentration). The other is surface diffusion of C around the particle (black dashed arrows). The diffusion speed and the distance to be traveled determine the growth mode of CNTs. (b) Root-growth mode. If the surface diffusion is faster than diffusion through the particle, the particle–surface will be readily saturated and nucleation of C around the periphery of the particle will lead to root-growth. The particle serves as a template for growth and remains on the substrate during the growth. (c) Tip-growth mode. If the bulk diffusion is faster than the surface diffusion, the C will build up most rapidly at the catalyst–substrate interface, precipitate at the interface, and start formation of a NT. The particle remains at the tip of the NT during the growth.

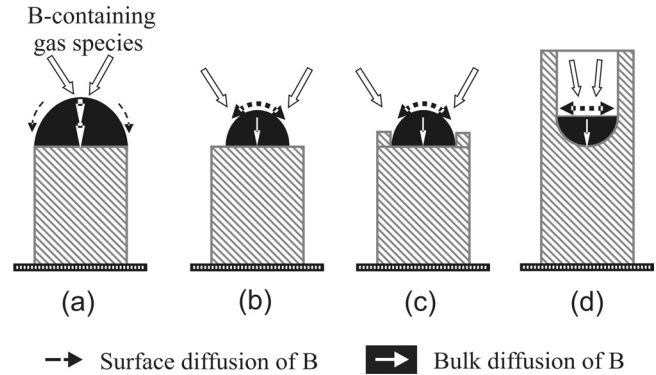


Fig. 4. Hypothesis 1 for growth of B hybrid nanostructures. (a) Growth of a B nanowire according to the VLS mechanism (“tip-growth mode”). (b) Reduction in size of the catalytic particle to create new nucleation sites. (c) B precipitates around the periphery of the catalytic particle. The growth mode changes from tip-growth to root-growth. (d) Final formation of *tube-catalytic particle-wire* hybrid B nanostructures.

mechanism (Fig. 4(a)). (ii) Size reduction of catalytic particles to create new nucleation sites. Nanoparticles can shrink at high temperature due to evaporation; the metal in the nanoparticles is not in equilibrium in the reaction chamber, and one expects a net flux away from the nanoparticles as a function of time. It has been reported that nanoparticles can have much lower melting temperatures than the bulk material, and one might expect that their evaporation rate also exceeds that of the bulk particles that are (also) not in equilibrium, for example. In addition, the catalytic particles may also change their size and/or shape due to, e.g., surface tension and interface wetting effects. As the catalytic particles shrink, new nucleation sites along their periphery could be created (Fig. 4(b)). (iii) Growth of tubular portions. The (assumed) size reduction not only creates new nucleation sites, but also is likely to leave the particle surface saturated with B. The rate of surface saturation of boron might be much faster than that of boron penetration into the liquid–solid interface. Therefore, boron precipitated at the catalytic particle surface (or periphery) could provide a nanoscale template for nanotube nucleation. In other words, the growth mechanism transforms from tip to root growth (Fig. 4(c)). (iv) Final formation of the *tube-catalytic particle-wire* hybrid boron nanostructures (Fig. 4(d)). The shape change of the catalytic particle might be related to a change of wettability between the catalytic particle and the surrounding boron as a function of time.

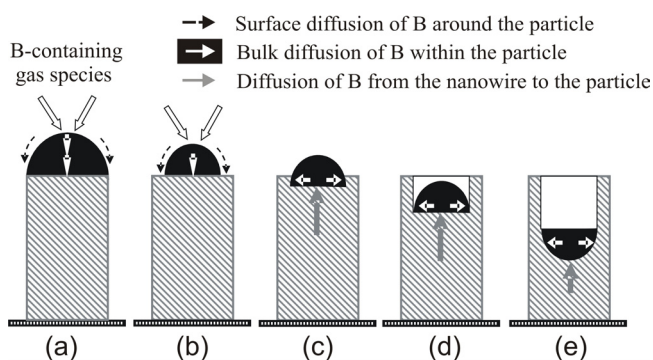


Fig. 5. Hypothesis 2 for growth of B hybrid nanostructures. (a) Growth of a B nanowire according to the VLS mechanism. (b) Size reduction of the catalytic particle to create new nucleation sites along the periphery of the particle. (c) Diffusion of B from nanowire to particle (indicated by gray arrow) to make the particle saturated with B, followed by precipitation of B at the new nucleation sites, and initiation of the tubular structure growth. [(d) and (e)] Formation of final *tube-catalytic particle-wire* hybrid B nanostructure. The growth of the tubular portion can also be thought of in terms of the catalytic particle “migrating downwards”.

**Hypothesis 2.** The hybrid nanostructures were formed after the  $B_2H_6$  precursor was turned off (i.e., during the cooling process under Ar).

In this hypothesis, five major steps are suggested. The first two steps are similar to those in Hypothesis 1. They are (i) VLS growth of a B nanowire (Fig. 5(a)), and (ii) size reduction of the catalytic particle (Fig. 5(b)). The size reduction of the catalytic particles produces new nucleation sites along the periphery of the catalytic particle. (iii) If the  $B_2H_6$  precursor is turned off after Step ii, the concentration difference of B in the catalytic particle versus in the B nanowire will promote B diffusion from the B nanowire to the catalytic particle (gray arrow in Fig. 5(c)). (iv) Eventually, the catalytic particle supersaturates with B and precipitates at new nucleation sites along the periphery of the catalytic particle, forming a tubular structure (Figs. 5(d) and 5(e)). In this scenario, the wire portion of the hybrid nanostructure itself is the source of B for growth of the tubular portion. (v) The length increase of the tubular portion can thus be considered as the result of “migration” of the catalytic particle “downwards” (Fig. 5(e)).

To further explore each hypothesis, two different annealing tests were carried out: (i) Post-annealing test. After the as-synthesized samples were subjected to SEM examination, they were re-inserted into the reaction chamber and subjected

to a high temperature treatment at  $900^\circ\text{C}$  (ramp-up time: 1 hr) under 20 sccm Ar flow for 2 h (the chamber pressure was adjusted to  $\sim 200$  mTorr with a butterfly valve). The samples were then cooled down to room temperature under Ar flow ( $\sim 5$  h), and removed for SEM examination. Figure 6(a) is a typical SEM picture, showing the morphology of B nanostructures after this high temperature treatment under inert gas. No clear *tube-catalytic particle-wire* hybrid B nanostructures can be observed in this picture. Instead, the B nanostructures seem to be “transparent” and hollow throughout. Some nanostructures have open ends (indicated by white arrows). Since these high temperature treated (under inert gas) samples were

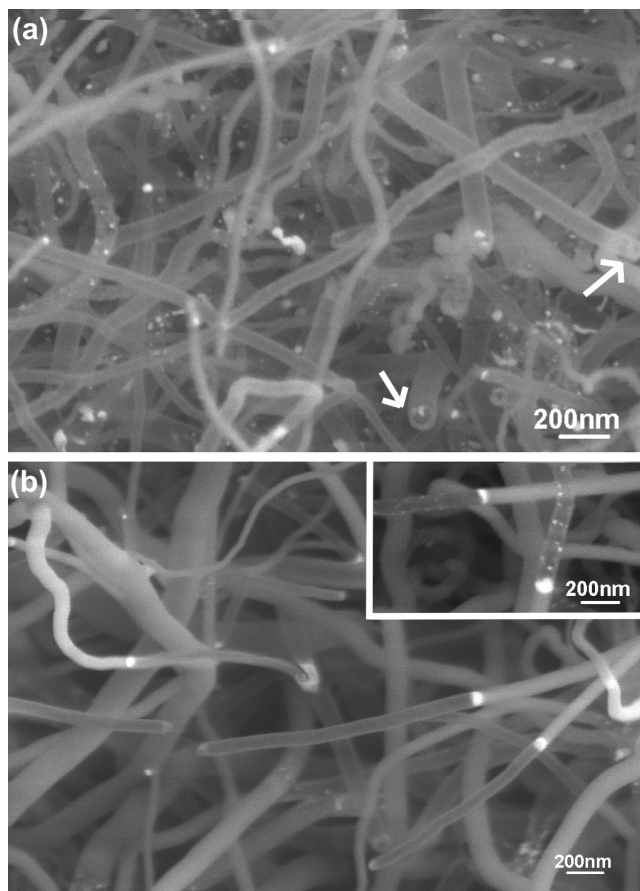


Fig. 6. SEM micrographs of (a) B nanostructures after sample extraction and re-insertion, and high temperature exposure as described in the text. No clear *tube-catalytic particle-wire* hybrid nanostructures can be observed. The B nanostructures seem to be “transparent” and hollow. Some nanostructures have open ends (indicated by white arrows). (b) B nanostructures after *in situ* annealing. Note the longer tube segments of the *tube-catalytic particle-wire* hybrid nanostructures. The inset shows what appear to be small “Au” particles on the inner wall of the tube segments.

exposed to the atmosphere beforehand, molecular adsorbates could adsorb on the B nanostructures and perhaps complicate the final annealing results. Therefore, we decided to perform an *in situ* annealing test. (ii) *In situ* annealing test. After the sample coupons were exposed to B<sub>2</sub>H<sub>6</sub>, the B<sub>2</sub>H<sub>6</sub> was turned off and the coupons were held at 900°C in 20 sccm Ar for 2 h. Figure 6(b) is a typical SEM micrograph, showing the morphology of the *tube-catalytic particle-wire* hybrid B nanostructures after this *in situ* annealing. The lengths of the tube segments of these “annealed” B hybrid nanostructures are  $\sim 1.5 \mu\text{m}$ . Compared to the length of the tube segments of as-synthesized B hybrid nanostructures ( $\ll 1 \mu\text{m}$ ), the typical length of the tube segments in the as-annealed B hybrid nanostructures is clearly increased. In addition, on some inner walls of tube segments (inset, Fig. 6(b)), traces of Au can be observed, suggesting the migration of Au at higher temperature. These experimental results seem to support Hypothesis 2. To further understand the evolution of the tube section, a high temperature *in situ* TEM (or SEM) study would be useful.

## 5. Summary

In summary, catalyst-assisted growth of nanowires of B that were primarily amorphous and *tube-catalytic particle-wire* hybrid B nanostructures by pyrolysis of B<sub>2</sub>H<sub>6</sub> at 820–890°C and  $\sim 200$  mTorr was achieved using a home-built LPCVD system. Au, and an alloy of Pt/Pd, are effective catalysts. Growth of amorphous boron nanowires is probably due to the VLS mechanism, aided by the presence in the metal catalyst (e.g., Au) of Si, or in a separate case, of Al. Two possible growth mechanisms for the novel *tube-catalytic particle-wire* hybrid B nanostructures were presented, and one of them is supported over the other by annealing experiments in the absence of B<sub>2</sub>H<sub>6</sub>. We suggest that these hybrid B nanostructures might have a novel application in composites, in that the tubular portion might “interlock” particularly well with a variety of different matrix types.

## Acknowledgments

We appreciate the support of the National Science Foundation (RSR: grant EEC-0210120). We are grateful to the NUANCE facility at Northwestern University for supplying multi-user SEM and TEM

instruments, and the RRC facility at the University of Illinois-Chicago for supplying multi-user TEM instruments used in these studies.

## References

1. R. M. Adams, *Boron, Metallo-Boron, Compounds and Boranes* (Interscience Publishers, New York, 1964).
2. V. I. Matkovich, *Boron and Refractory Borides* (Springer-Verlag, Berlin, 1977).
3. N. N. Greenwood and A. Earnshaw, *Chemistry of the Elements* (Reed Educational and Professional Publishing Ltd., UK, 1997).
4. J. E. Bailey, *Handbook of Polymer-Fibre Composites*, ed. F. R. Jones (Longman Scientific & Technical, Harlow, UK, 1994), p. 15.
5. F. N. Tavazde, Y. V. Lominadze, A. G. Khvedelidze, G. V. Tsagareishvili, M. K. Shorshorov and S. I. Bulichev, *J. Less-Common Met.* **82**, 95 (1981).
6. I. Boustani, *J. Solid State Chem.* **133**, 182 (1997).
7. I. Boustani, *Surf. Sci.* **370**, 355 (1997).
8. I. Boustani and A. Quandt, *Europhys. Lett.* **39**, 527 (1997).
9. I. Boustani, A. Quandt, E. Hernandez and A. Rubio, *J. Chem. Phys.* **110**, 3176 (1999).
10. A. Quandt, A. Y. Liu and I. Boustani, *Phys. Rev. B* **6412**, 125422/1 (2001).
11. L. M. Cao, Z. Zhang, L. L. Sun, C. X. Gao, M. He, Y. Q. Wang, Y. C. Li, X. Y. Zhang, G. Li, J. Zhang and W. K. Wang, *Adv. Mater.* **13**, 1701 (2001).
12. X. M. Meng, J. Q. Hu, Y. Jiang, C. S. Lee and S. T. Lee, *Chem. Phys. Lett.* **370**, 825 (2003).
13. C. J. Otten, O. R. Lourie, M. F. Yu, J. M. Cowley, M. J. Dyer, R. S. Ruoff and W. E. Buhro, *J. Am. Chem. Soc.* **124**, 4564 (2002).
14. Y. Q. Wang and X. F. Duan, *Appl. Phys. Lett.* **82**, 272 (2003).
15. Q. Yang, J. Sha, J. Xu, Y. J. Ji, X. Y. Ma, J. J. Niu, H. Q. Hua and D. R. Yang, *Chem. Phys. Lett.* **379**, 87 (2003).
16. J. Z. Wu, S. H. Yun, A. Dibos, D. K. Kim and M. Tidrow, *Microelectr. J.* **34**, 463 (2003).
17. Y. J. Zhang, H. Ago, M. Yumura, T. Komatsu, S. Ohshima, K. Uchida and S. Iijima, *Chem. Commun.* **23**, 2806 (2002).
18. Z. K. Wang, Y. Shimizu, T. Sasaki, K. Kawaguchi, K. Kimura and N. Koshizaki, *Chem. Phys. Lett.* **368**, 663 (2003).
19. T. T. Xu, J.-G. Zheng, N. Wu, A. W. Nicholls, J. R. Roth, D. A. Dikin and R. S. Ruoff, *Nano Lett.* **4**, 963 (2004).
20. J. Ma, Y. Gu, L. Shi, L. Chen, Z. Yang and Y. Qian, *Chem. Phys. Lett.* **381**, 194 (2003).
21. Y. Y. Wu, B. Messer and P. D. Yang, *Adv. Mater.* **13**, 1487 (2001).

22. Q. Yang, S. Jian, X. Ma, Y. Ji and D. Yang, *Superconductor Sci. Tech.* **17**, L31 (2004).
23. R. Ma, Y. Bando, T. Mori and D. Golberg, *Chem. Mater.* **15**, 3194 (2003).
24. T. T. Xu, J.-G. Zheng, A. W. Nicholls, S. Stankovich, R. D. Piner and R. S. Ruoff, *Nano Lett.* **4**, 2051 (2004).
25. H. Zhang, Q. Zhang, J. Tang and L.-C. Qin, *J. Am. Chem. Soc.* **127**, 2862 (2005).
26. H. Zhang, Q. Zhang, J. Tang and L.-C. Qin, *J. Am. Chem. Soc.* **127**, 8002 (2005).
27. H. Zhang, Q. Zhang, G. Zhao, J. Tang, O. Zhou and L.-C. Qin, *J. Am. Chem. Soc.* **127**, 13120 (2005).
28. Y. Zhang, T. Ichihashi, E. Landree, F. Nihey and S. Iijima, *Science* **285**, 1719 (1999).
29. J. Hu, M. Ouyang, P. Yang and C. M. Lieber, *Nature* **399**, 48 (1999).
30. R. S. Wagner and W. C. Ellis, *Trans. Metall. Soc. AIME* **233**, 1053 (1965).
31. Z. Wang, Y. Shimizu, T. Sasaki, K. Kirihara, K. Kawaguchi, K. Kimura and N. Koshizaki, *J. Solid State Chem.* **177**, 1639 (2004).
32. H. Cooper, *Rare Metals Handbook*, ed. C. A. Hampel (Reinhold Publishing Corporation, London, 1954), p. 71.
33. Y. Li, R. S. Ruoff and R. P. H. Chang, *Chem. Mater.* **15**, 3276 (2003).
34. H. C. Longuet-Higgins and M. D. V. Roberts, *Proc. R. Soc. A* **230**, 110 (1955).
35. H. Okamoto, *Desk Handbook: Phase Diagrams for Binary Alloys* (ASM International, Materials Park, OH, 2000).
36. F. Wald and R. W. Stormont, *J. Less-Common Met.* **9**, 423 (1965).
37. S. Motojima, F. Sugimori, Y. Takahashi and K. Sugiyama, *Denki Kagaku* **43**, 323 (1975).
38. W. J. Croft, N. C. Tombs and J. F. Foltzgerald, *Mat. Res. Bull.* **5**, 489 (1970).
39. R. Ellis, *Boron, Synthesis, Structure, and Properties*, eds. J. A. Kohn, W. F. Nye and G. K. Gaule (Plenum Press, New York, 1960), p. 42.
40. O. A. Louchev, Y. Sato and H. Kanda, *Appl. Phys. Lett.* **80**, 2752 (2002).